ResearchGate

See discussions, stats, and author profiles for this publication at: https://www.researchgate.net/publication/317472628

Estimates of plant density of wheat crops at emergence from very low altitude UAV imagery

Article *in* Remote Sensing of Environment · June 2017
DOI: 10.1016/j.rse.2017.06.007

CITATIONS
15

READS
1,136

5 authors, including:

Xiuliang Jin
French National Institute for Agricultural Research
63 PUBLICATIONS **296** CITATIONS
SEE PROFILE

Shouyang Liu
French National Institute for Agricultural Research
13 PUBLICATIONS **65** CITATIONS
SEE PROFILE

Baret Frederic
French National Institute for Agricultural Research
400 PUBLICATIONS **19,249** CITATIONS
SEE PROFILE

Matthieu Hemmerlé
Hiphen
6 PUBLICATIONS **32** CITATIONS
SEE PROFILE

Some of the authors of this publication are also working on these related projects:

GEOLAND2 View project

Vegetation indices View project

All content following this page was uploaded by Xiuliang Jin on 09 October 2017.

The user has requested enhancement of the downloaded file.

Remote Sensing of Environment 198 (2017) 105–114

Contents lists available at ScienceDirect

Remote Sensing of Environment

journal homepage: www.elsevier.com/locate/rse

Estimates of plant density of wheat crops at emergence from very low altitude UAV imagery

Xiuliang Jin [a,*], Shouyang Liu [a], Frédéric Baret [a], Matthieu Hemerlé [b], Alexis Comar [b]

[a] UMR EMMAH, INRA, UAPV, 84914 Avignon, France
[b] HIPHEN, 84914 Avignon, France

ARTICLE INFO

Article history:
Received 11 October 2016
Received in revised form 24 May 2017
Accepted 3 June 2017
Available online xxxx

Keywords:
Plant density
Unmanned aerial vehicle
Computer vision algorithm
Particle swarm optimization (PSO)-support vector machine (SVM)
Winter wheat

ABSTRACT

Plant density is useful variable that determines the fate of the wheat crop. The most commonly used method for plant density quantification is based on visual counting from ground level. The objective of this study is to develop and evaluate a method for estimating wheat plant density at the emergence stage based on high resolution imagery taken from UAV at very low altitude with application to high throughput phenotyping in field conditions. A Sony ILCE α5100L RGB camera with 24 Mpixels and equipped with a 60 mm focal length lens was flying aboard an hexacopter at 3 to 7 m altitude at about 1 m/s speed. This allows getting ground resolution between 0.20 mm to 0.45 mm, while providing 59–77% overlap between images. The camera was looking with 45° zenith angle in a compass direction perpendicular to the row direction to maximize the cross section viewed of the plants and minimize the effect of the wind created by the rotors. Agisoft photoscan software was then used to derive the position of the cameras for each image. Images were then projected on the ground surface to finally extract subsamples used to estimate the plant density. The extracted images were first classified to separate the green pixels from the background and the rows were then identified and extracted. Finally, image object (group of connected green pixels) was identified on each row and the number of plants they contain was estimated using a Support Vector Machine whose training was optimized using a Particle Swarm Optimization.

Three experiments were conducted in Gréoux, Avignon and Clermont sites with some variability in the sowing dates, densities, genotypes, flight altitude, and growth stage at the time of the image acquisition. The application of the method on the 270 samples available over the three sites provides a RMSE and relative RMSE on estimates of 34.05 plants/m^2 and 14.31% with a bias of 9.01 plants/m^2. However, differences in performances were observed between the three sites, mostly related to the growth stage at the time of the flight. Plants should have between one to two leaves when images are taken. Further, a specific sensitivity analysis shows that the ground resolution of the images should be better than 0.40 mm. Finally, the repeatability of the method is good especially when images are taken from similar observational geometries. The current limits and possible improvements of the method proposed are finally discussed.

© 2017 Elsevier Inc. All rights reserved.

1. Introduction

Plant density is a key factor influencing crop functioning with consequences on many aspects including yield, water and fertilizer requirements as well as susceptibility to pathogens. Previous research on winter wheat showed that the plant density was related to the green fraction, the accumulated dry matter and the yield (Joseph et al., 1985; Whaley et al., 2000). However, the tillering capacity of wheat crops allows to partly compensate the variability in plant density. This resilience to changes in plant density depends on the environmental conditions as well as on the genotypic characteristics. Plant breeders are thus eager to characterize the tillering capacity of genotypes using the tillering coefficient, i.e. the average number of tillers per plant. It is generally computed at harvest by dividing the number of ears per unit area by the corresponding plant density. Plant density is therefore receiving great attention within plant breeding programs.

The current methods used are based on visual plant counting in the fields over a predefined sampling area. They are tedious, time consuming and prone to human errors. Further, the soil conditions, particularly in case of rainfall or frost, may limit the time slots when walking in the field is possible without damaging the crop. Therefore, it is difficult to measure the plant density using such manual method when applied to large fields for documenting the spatial variability, or when applied to large phenotyping experiments with several hundred to several

* Corresponding author.
E-mail addresses: xiuliang.jin@inra.fr, jinxiuxiuliang@126.com (X. Jin).

http://dx.doi.org/10.1016/j.rse.2017.06.007
0034-4257/© 2017 Elsevier Inc. All rights reserved.

thousands of microplots to be characterized. It is thus necessary to develop alternative methods to provide timely and accurate quantification of the plant density.

The fast and recent development of sensors and computer vision algorithms provides new opportunities to estimate plant density with non-intrusive methods. Most studies on plant density estimation are using ground level non-contact measurements, mainly focusing on relatively large plants such as maize that are further regularly spaced. Most techniques are based on plant identification using RGB images (Jia et al., 1991; Nakarmi and Tang, 2012; Nakarmi and Tang, 2014; Shrestha and Steward, 2003; Shrestha and Steward, 2005; Tang and Tian, 2008a; Tang and Tian, 2008b), or LiDAR systems (Shi et al., 2015). However, little attention was paid to crops such as wheat having small and variable spacing between plants on the row with relatively narrow leaves. Maertens et al. (2003) used an ultrasonic transducer that was found to be both sensitive to the volumetric density and to the crop architecture. Saeys et al. (2009) used a LiDAR to estimate with success plant density of small grain crops such as wheat. From our knowledge, no other studies report attempts to estimate the plant density by non-destructive methods over wheat crops.

Recent technological advances resulted in a boom in the development of Unmanned Aerial Vehicle (UAV). In addition, with the development of versatile, lightweight, and low-cost portable sensors, UAVs may be transformed into remote sensing platforms that provide images with high spatial resolution. Further, UAV allows more flexibility in the acquisition time with no constraints on the soil conditions that may limit rover systems equipped with cameras or operator walking on the ground for visual counting. Therefore, UAV is a promising remote sensing platform that gained a lot of attention for a range of scientific or application oriented uses. UAVs are becoming a standard tool for crop production managers who exploit the high spatial and temporal resolution to quantify in-field crops variation (Ehsani and Maja, 2013; Gómez-Candón et al., 2014). A review of the use of UAVs for precision agriculture was provided by Zhang and Kovacs (2012) while Sankaran et al. (2015b) focused on phenotyping applications. Imagery from UAV coming from different sensors [RGB (Red Green Blue) cameras, multispectral imagery, hyperspectral imagery, and thermal camera] have been used to estimate LAI (Hunt et al., 2008; Hunt et al., 2010; Verger et al., 2014), the fraction of intercepted photosynthetically active radiation (Guillen-Climent et al., 2012), biomass (Bendig et al., 2015; Hunt et al., 2005), height (Bendig et al., 2015; Díaz-Varela et al., 2015), nitrogen (Hunt et al., 2005), carotenoid (Zarco-Tejada et al., 2013), and temperature (Sullivan et al., 2007; Zarco-Tejada et al., 2012). More recently, Sankaran et al. (2015a) used a multispectral camera to evaluate emergence and spring survival rates of wheat from UAV observations using a vegetation index.

This brief review demonstrates that only little attention was devoted to non-invasive methods for estimating plant density in wheat crops. Recently, Liu et al. (2017) have proposed a method for wheat plant counting at emergence based on high spatial resolution RGB images taken from the ground level either from a rover system or from handheld cameras. The transposition of this method to observations from UAV would be very appealing to reach the high throughput required for field phenotyping (Araus and Cairns, 2014; Furbank and Tester, 2011; Walter et al., 2015). Further, UAVs ensure the desired flexibility needed for such application and is fully independent from the trafficability of the soil.

The main objective of this study is to adapt to UAV observations the method developed by Liu et al. (2017) for plant density estimation and to evaluate the associated estimation accuracy. The experiments are first presented along with the algorithm developed to estimate the plant density. The performances of the method are then evaluated with emphasis on repeatability and the impact of the spatial resolution that may be a limiting factor for UAV observations. Finally, conclusions are drawn on the adequacy of the proposed method for precision farming and phenotyping applications.

2. Materials and methods

2.1. The experimental sites

Three experimental sites with winter wheat crops were considered: Gréoux, Avignon and Clermont (Table 1). The Gréoux and Avignon sites are in southeast France with a typical Mediterranean climate. The Clermont site is in the center of France, with a more continental climate. The Gréoux and Clermont sites were hosting genotype experiments with respectively 111 and 2304 microplots. The microplots in Gréoux were 10 m long with 13 rows. Those of Clermont were 2.5 m long with 8 rows. A total of 37 and 228 microplots were sampled respectively in Gréoux and Clermont. In Avignon, a single field with single genotype was sampled over 30 microplots. The nominal sowing density, sowing dates and row spacing are indicated in Table 1.

2.2. UAV and flight characteristics

A hexacopter developed by Atechsys (http://atechsys.fr/) was used to carry a high resolution RGB camera. The camera was viewing the crop from a 45° zenith angle in a compass direction perpendicular to the row direction to maximize the cross section of the plants. The camera was set up on a 2 axes gimbal that maintains automatically the orientation of the camera independently from the movement of the UAV. Note that the 45° inclination of the camera allows the UAV to observe the microplot from a horizontal distance equal to the altitude: the wind created by the rotors was therefore blowing on another microplot rather than the one currently observed. The UAV trajectory was prepared before the flight to get 59%–77% overlap of the image footprint along and across tracks (Table 2). The trajectory was then controlled automatically by the GPS within an accuracy around 2 m for the horizontal position and by the barometer for the altitude within around 0.5 m accuracy. The UAV was flying at about 1 m/s speed at an altitude of 3 m to 7 m depending on the sites (Table 2). The autonomy of the system is around 12 min and several flights (2 to 4) were necessary to cover the ensemble of microplots for the Gréoux and Clermont sites. Note that 2 flights were completed in Avignon with 2 different altitudes (Table 2).

Circular panels of 20 cm diameter were distributed in the field to be used as ground control points (GCPs) to get more accurate positioning of the images. The center of each panel was located with a centimeter accuracy using a RTK GPS system (Trimble Geo 7×). The flights were completed around Haun stage 1.0–2.5 (Haun, 1973) for the three sites (Table 2). These early stages correspond to 1.0 to 2.5 visible leaves when the overlap between neighbor plants is limited to ease plant identification. Measurements were completed mostly under cloudy illumination conditions, with light to moderate wind.

2.3. The camera and image extraction over microplots

A Sony ILCE α5100L RGB camera with 6024 × 4024 pixels was installed on the UAV. The camera uses a CMOS sensor of 23.5 × 15.6 mm with a pixel size of 3.88 μm. The camera was equipped with a 60 mm focal length lens to increase the spatial resolution while keeping at a reasonable flight altitude (3 m, 5 m and 7 m). The camera was set to speed priority with auto adjustment of the ISO up to a maximum of ISO = 1600. The images were recorded in raw format (ARW) on the SD memory card. Images were acquired at 1 Hz frequency using an intervalometer that triggers the camera. Images were then downloaded after each flight and saved in TIF format using the open-source DCRaw software (http://www.cybercom.net/~dcoffin/dcraw/).

For each experiment, the TIF images available were processed using Agisoft Photoscan Professional edition (Version 1.2.2, Agisoft LLC., Russia). The software computes the position of the camera corresponding to each image acquired if the overlap between images is larger than 60% (Agisoft LLC, 2016). The flight plan associated to the camera field of view and image acquisition frequency was providing a sufficient

Table 1
Location of the Gréoux, Avignon and Clermont experimental sites, along with the sowing date, sowing density and row spacing.

Sites	Latitude	Longitude	Number of microplots	Sowing date	Nominal sowing density (seeds/m^2)	Row spacing (cm)
Gréoux	43°45′N	5°53′E	20	28/10/2014	300	17.5
Avignon	43°57′N	4°49′E	30	13/11/2015	395	15.2
Clermont	45°46′N	3°70′E	50	12/11/2015	280	16.4

overlap on most situations (Table 2). The software recognizes automatically the circular panels used as GCP for absolute geopositioning of the images and locates their center precisely on the images. The accuracy achieved for the positioning of the images was around 2.3 cm as evaluated over the GCPs using a cross validation leave-one out process. The plant density estimation was completed over a subsample of each microplot. The size of the subsample was varying among the three sites (Table 2). The coordinates of the subsample over each microplot were manually defined using the orthomosaic image generated by the Agisoft Photoscan software. Note that several subsamples could be extracted from the same microplot. The orthomosaic degrades significantly the quality of the original images which prevents from properly identifying plants. It was therefore preferred to work on the original images. For this purpose, the Phenoscript software (Version 0.8.2, developed by our team) was used to extract the subsamples of the microplot from each image and to project them onto the ground to get orthorectified images, assuming that the ground surface was flat and horizontal. Because of the ortho-rectification applied to the images, distances in pixels in the image can be simply converted into actual metric distances using the scale factor computed by Phenoscript. Each undistorted (orthorectified) image was associated to the corresponding ground resolution computed by Phenoscript. Several images may contain the same subsample viewed from different positions. For each subsample, the image extract providing the best quality (no blur), fully containing the subsample and the closest to the targeted view direction (45° zenith angle and compass orientation perpendicular to the row direction) was selected. The flowchart of data processing for UAV image data is shown in Fig. 1.

2.4. Data processing

The data processing is mainly composed of three steps: (1) images of the subsample extract are first classified and the rows extracted; (2) then, image objects (group of connected green pixels) along the row are identified and characterized by a set of features; (3) finally each image object is classified according to the number of plants it includes. These three steps are described hereafter and illustrated in Fig. 2.

2.4.1. Classification and row extraction

The selected subsample image was then first classified to separate the green pixels from the background. This was achieved using the method proposed by Meyer and Neto (2008) which was demonstrated to perform better than the Otsu automatic thresholding (Otsu, 1979) applied to a vegetation index as considered in Liu et al. (2017). A vegetation index called MNVI is first computed for each pixel using the three colors [R, G, B] of the RGB image: MNVI is the difference between the excess green (EGVI = 2G-R-B) and excess red (ERVI = 1.4R-B) vegetation indices: MNVI = EGVI-ERVI = 2G-2B-2.4R. The positive MNVI values correspond to the green pixels and negative values to the background. The MNVI images were thus transformed into binary images using MNVI = 0 as a threshold value and assigning 1 to the green pixels and 0 to the background. Possible weeds were eliminated from the binary image by removing objects with <30 connected pixels using an area opening algorithm (Ahmed et al., 2008).

The Hough transform (Hough, 1962) was applied to get the orientation of the main elements. The subsample image was then rotated accordingly using the nearest neighbor interpolation method, the row direction being parallel to the x axis of the image. An example on the rotated original image and the corresponding binary one is displayed in Fig. 3. The row positions are then identified by the peaks across the row direction of the sum of the green pixels computed along the row direction. The three rows in the center of the image are then extracted from each subsample image for Gréoux and Clermont, while only two rows were considered for the Avignon site for which the image footprint was relatively small.

2.4.2. Object identification and characterization

Image objects are identified using the MATLAB function bwlabel (Haralick and Shapiro, 1992). Each image object is then characterized by a set of 13 features described in table and computed with the regionprops function of MATLAB software (version 2015b, MathWorks, USA).

2.4.3. Object classification

For each site, a supervised classification was conducted to estimate the number of plants inside each image object. For this purpose, the plants were identified by interactively clicking on the bottom of the plants on the images of the 2 or 3 central rows considered. This process although tedious was relatively easy due to the good quality of images and would be associated with very little uncertainties. A Support Vector Machine (SVM) method (Vapnik, 2013; Vapnik and Vapnik, 1998) was then trained to relate the 13 image object features (Table 3) to the number of plants inside each image object assessed visually. The SVM machine learning method was used here conversely to the neural network approach proposed by Liu et al. (2017) because SVMs are recognized to generalize well in case of limited training dataset (Mountrakis et al., 2011). A radial basis function was used because this kernel adapts well to a large range of problems by varying the scaling factor. The punishment (C) and kernel function parameters (γ) used in the SVM algorithm were tuned using a particle swarm optimization (PSO) algorithm (Kenndy and Eberhart, 1995). This iterative algorithm starts with an ensemble of possible solutions called particles. Initial velocities are also associated to each particle: they correspond to the change of position of the particle in the solution space between two iterations. Trapping in a local minimum is avoided by considering both the global minimum over all particles and the individual minimum of

Table 2
Summary of the main flight characteristics for three experimental sites.

Sites	Date of flight	Haun stage	Altitude (m)	Ground resolution (mm)	Overlap (along/across)	Size of subsample
Gréoux @3 m	11/11/2014	1.5	3	0.20	38%/80%	1.5 m × 3rows
Avignon @5 m	14/12/2015	2.5	5	0.33	62%/80%	0.5 m × 2rows
Avignon @7 m	14/12/2015	2.5	7	0.45	73%/80%	0.5 m × 2rows
Clermont @7 m	22/12/2015	1.0	7	0.45	73%/80%	2.5 m × 3rows

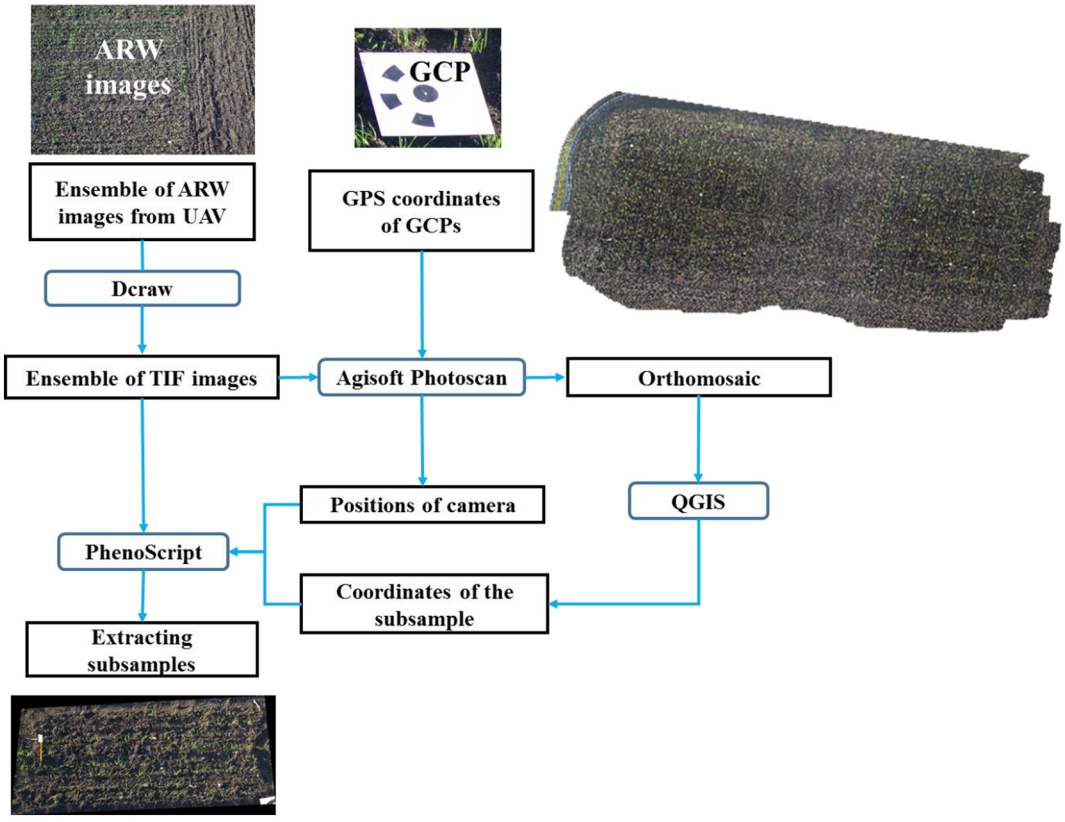

Fig. 1. The flowchart of data preprocessing for UAV images.

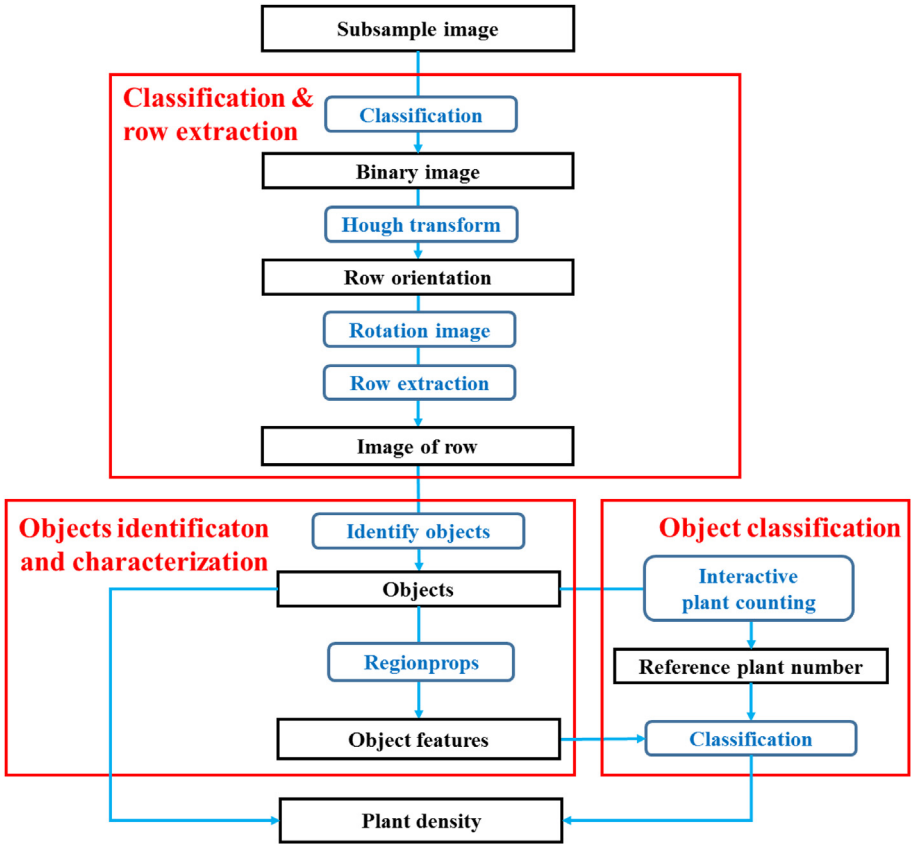

Fig. 2. The schematic diagram of data processing for estimating plant density of winter wheat.

(a) (b)

Fig. 3. The classification result using an improved color vegetation index with an automatic thresholding: (a) original image and (b) classification binary image.

each particle along its trajectory. At each iteration, the position of the particles and associated velocities are updated up to the point when the convergence criterion is satisfied. The PSO-SVM method used here requires therefore three main steps:

(1) Initial configuration, including setting group size (25), number of iterations (300), the velocity of initial particle ($c1 = 1.5$, $c2 = 1.7$), the minimum and maximum values of parameters C ($0.01 < C < 1000$) and γ ($0.01 < \gamma < 1000$) for the SVM;
(2) Each particle corresponding to a couple of [C,γ] values was used to train the SVM prediction model. A fitness value is computed to evaluate the corresponding performances;
(3) The particle providing the best prediction power is finally selected.

Once the SVM is trained, it is applied to associate to each image object the corresponding number of plants. Finally, the number of plants for each subsample is then computed, and the corresponding density calculated by dividing by the subsample area.

2.5. Statistical analysis

For each site, the dataset is randomly divided into a calibration and a validation datasets using SPSS software (16.0, SPSS, Chicago, IBM, USA) (Table 4): 2/3 of the total number of image objects is used to train the classifier (Calibration); the remaining 1/3 image objects are used to evaluate the performances (Validation).

Table 3
The 13 features used to characterize each image object.

Name	Unit	Meaning
Area	$Pixel^2$	Number of pixels for the connected component (object).
Convexarea	$Pixel^2$	Number of pixels within the convex hull, referring to the smallest convex polygon containing the region.
Eccentricity	–	Eccentricity of the ellipse that has the same second-moments as the region.
Equivdiameter	Pixel	Diameter of a circle with the same area as the region.
Extent	Pixel	Ratio of pixels in the region to the total within the bounding box, referring to the smallest rectangle containing the region.
Filledarea	$Pixel^2$	Number of pixels for the object with all the gaps filled.
Majoraxislength	Pixel	Length of the major axis of the ellipse with the same normalized second central moments as the region.
Minoraxislength	Pixel	Length of the minor axis of the ellipse with the same normalized second central moments as the region.
Orientation	°	Angle between the x-axis and the major axis of the ellipse that has the same second-moments as the region.
Solidity	–	Ratio of pixels in the region to the total within the convex hull.
Lengthskelet	Pixel	Number of pixels for the skeleton.
Numend	–	Number of end points for the skeleton.
Numbranch	–	Number of branch points for the skeleton.

Performances were evaluated using the coefficient of determination (R^2) and root mean square error (RMSE), relative root mean square error (RRMSE) (Wilson and Sagan, 1995). In addition, the index of agreement (d) proposed by (Willmott, 1982) was calculated:

$$d = 1 - \frac{\sum_{i=1}^{n}(E_i - M_i)^2}{\sum_{i=1}^{n}\left(|E_i - \overline{M}| + |M_i - \overline{M}|\right)^2} \quad (1)$$

where n is the number of samples, E_i and M_i are respectively the estimated and measured plant density values for sample i, and $\overline{M}$is the mean of measured plant density.

To evaluate the repeatability of the developed method, thirty subsamples were selected from the Clermont experimental site where central rows of these subsamples were imaged three times because of the overlap between consecutive images. These three extracts were used to evaluate the residuals quantified by the variability between the three estimates of the plant density:

$$Residual = E_i - \overline{E} \quad (2)$$

where $\overline{E}$is the mean estimated plant density from the three extracts E_i, $1 \le i \le 3$ of the same subsample.

3. Results and discussion

3.1. Evaluation of performances at the highest spatial resolution available

The performances evaluated over the validation data sets show only a slight degradation as compared to the calibration data set, providing some confidence on the robustness of the PSO-SVM method (Fig. 4 and Table 5). The estimated plant density is in good agreement with the corresponding measured one derived from visual identification of the plants in the image extracts for the Gréoux and Clermont sites (Fig. 4a, c and Table 5). However, performances of estimates degrade for the Avignon site (Fig. 4b). The bias between the estimated and the measured density values ranged from 2.59 plants/m^2 (Gréoux) to

Table 4
Summary of the measured plant density (plants/m^2) of winter wheat at the Gréoux, Avignon and Clermont experimental sites.

Sites	Dataset	Nb. subsamples	Min	Mean	Max	Range	SD[a]	CV[b] (%)
Gréoux	Calibration	40	90	204	297	207	59	29
@3 m	Validation	20	79	184	297	218	61	33
Avignon	Calibration	40	200	326	388	188	52	16
@5 m	Validation	20	223	306	388	165	45	15
Clermont	Calibration	100	133	230	278	145	36	16
@7 m	Validation	50	142	232	279	137	41	18
All	Calibration	180	90	245	388	298	64	26
	Validation	90	79	238	388	309	62	22

[a] SD, standard deviation.
[b] CV, coefficient of variation.

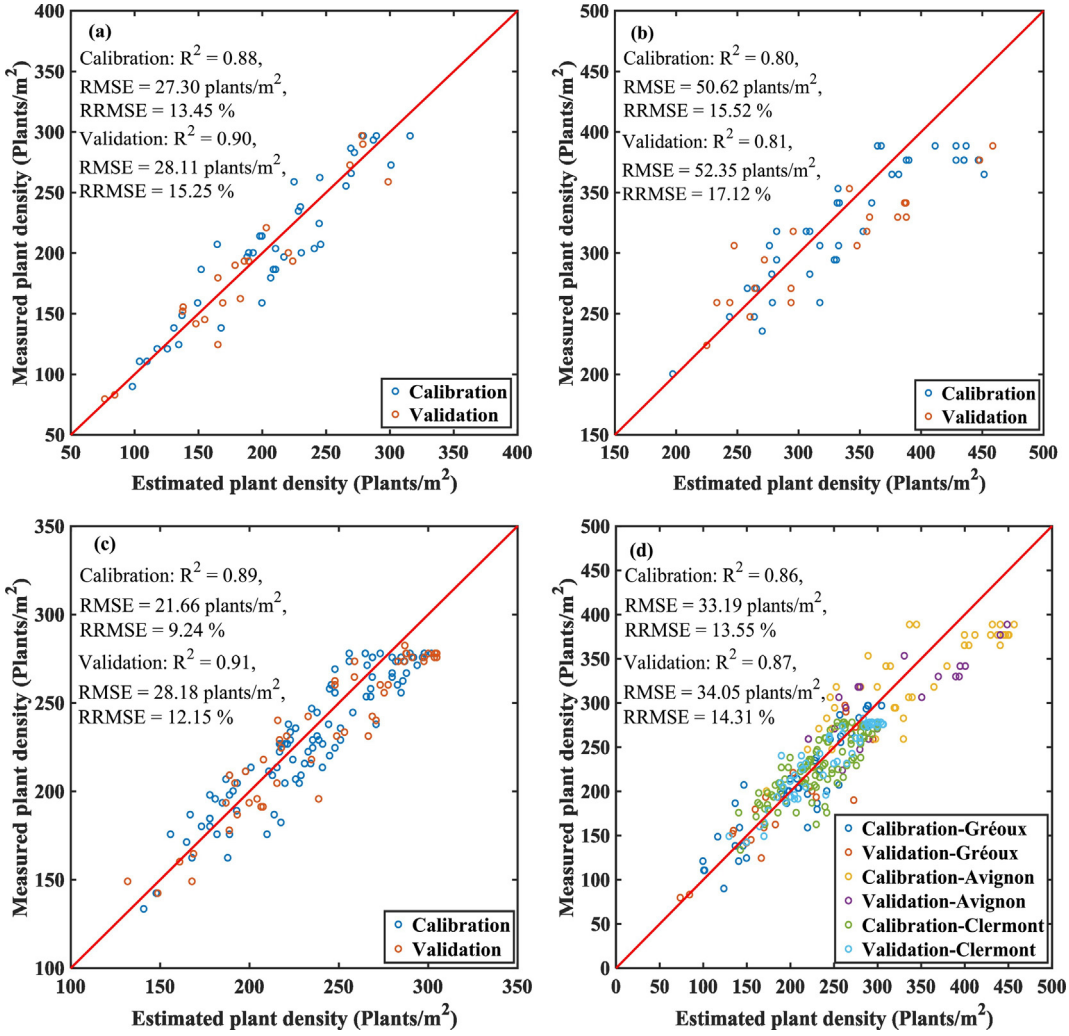

Fig. 4. Comparison between the estimated plant density using the highest spatial resolution RGB imagery with the corresponding measured values by visually identifying plants in the images. Data for the three experimental sites where calibration and validation data sets are well identified: (a) Gréoux @3 m, (b) Avignon @5 m, (c) Clermont @7 m, and (d) All.

15.90 plants/m^2 for Avignon (Table 5). The poorer performances observed in Avignon are mainly explained by the later Haun stage (2.5) when the UAV was flying over the crops as compared to Gréoux (1.5) and Clermont (1.0). The higher number of leaves corresponding to these later development stages makes more overlap between adjacent plants along the row. In these conditions, the image objects identified contain more plants and are thus more difficult to classify. This aspect may be even re-enforced by the fact that the plant density was significantly higher in the Avignon site (Table 4). The results suggested that the images should be taken at a Haun stage between 1 and 2 to minimize plant overlapping. The results of Jin and Tang (2009) also suggested that it was important to select the optimal growth stage to get accurate estimation of the plant density in maize crops.

The results showed that the maximum plant density estimated value is very consistent with the nominal sowing density (Tables 2 and 4, Fig. 4). The nominal sowing density targeted provides the potential density value. The actual density may decrease from the potential value depending on the emergence conditions. The difference between the estimated plant density and the measured one (Fig. 5) shows that the accuracy of estimated plant density degrades for the higher plant density. This is probably due to the increase overlap between consecutive plants that increases the number of image objects containing several plants which introduces additional difficulties and thus uncertainties as explained already earlier.

Our results are in very good agreement with those recently presented by Liu et al. (2017) based on RGB imagery taken from the ground

Table 5
Relationships between the estimated and measured plant density for winter wheat at three experimental sites.

Experimental sites	Dataset	Sample size	Slope	Intercept	R^2	RMSE (plants/m^2)	RRMSE (%)	d	Bias (plants/m^2)
Gréoux @3 m	Calibration	40	0.94	10.07	0.88	27.30	13.45	0.89	2.59
	Validation	20	0.95	5.49	0.90	28.11	15.25	0.90	3.68
Avignon @5 m	Calibration	40	0.69	89.02	0.80	50.62	15.52	0.81	15.90
	Validation	20	0.57	121.84	0.81	52.35	17.12	0.80	15.48
Clermont @7 m	Calibration	100	0.85	32.29	0.89	21.66	9.24	0.90	3.78
	Validation	50	0.83	34.41	0.91	28.18	12.15	0.92	7.85
All	Calibration	180	0.83	43.73	0.86	33.19	13.55	0.87	7.42
	Validation	90	0.80	53.91	0.87	34.05	14.31	0.87	9.01

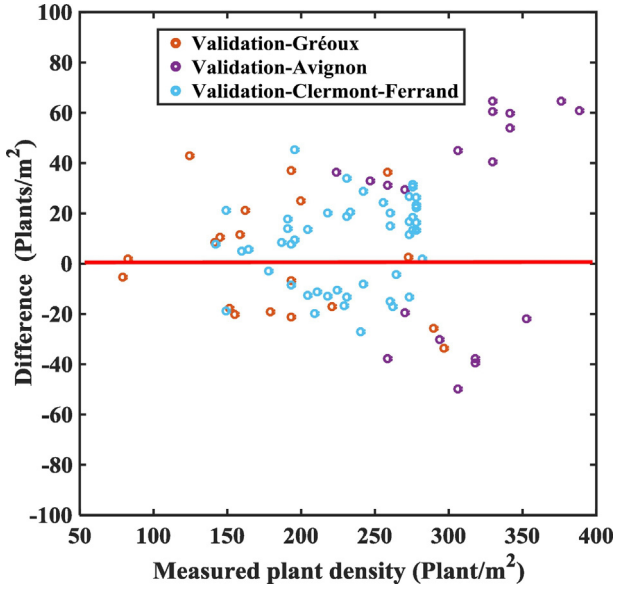

Fig. 5. Difference between the estimated plant density using the highest spatial resolution RGB imagery with the corresponding measured values at three experimental sites.

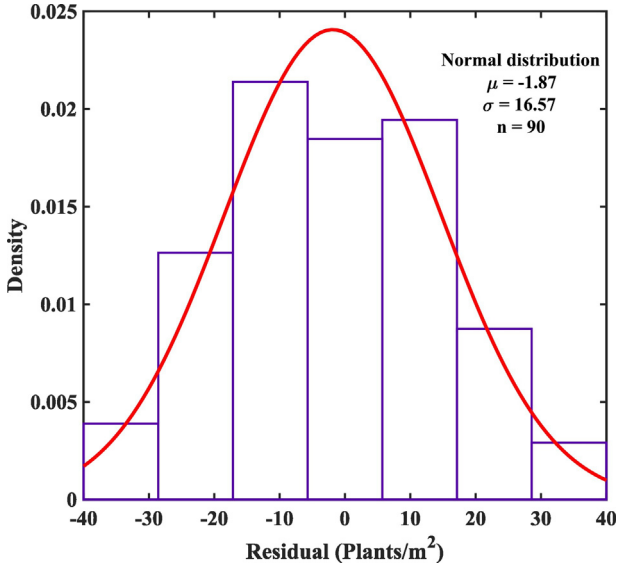

Fig. 6. Histogram (blue rectangles) showing the frequency of residual values of the estimates of plant density from the three different image extracts of the same subsample. The red curve shows the fitted normal distribution. The n is the number of dataset. (For interpretation of the references to color in this figure legend, the reader is referred to the web version of this article.)

level and reporting performances with RMSE ≈ 30 plants/m^2. It confirms that the same quality of images can be obtained from a UAV platform when flying at low altitude and speed. Improvement in the method for images with best quality and resolution would come mainly from the identification of the number of plants per image object. Our method is based on the morphological attributes of the image objects. Adding the RGB information would probably lead to marginal improvement since leaves at emergence appear to have a relatively homogenous green color. Further, their orientation close to the vertical induces only small variation in brightness. The representative features from images should be extracted using the more effective feature extracting methods. In addition, improvement would come from enhanced machine learning methods requiring larger training database.

Because of the relatively small number of samples, it was not possible to conduct a rigorous analysis of the residuals as a function of the genotypes. However, our visual observations indicate that only little variability is observed between genotypes at these early stages. Further, the training completed over the range of genotypes present in the trial would partly account for possible genotypic variability in the plant identification process. Additional studies should be carried out to propose a set of features that are little sensitive to possible genotypic differences.

3.2. Repeatability

Thirty subsamples with three different image extracts of the subsample were selected in the Clermont site to evaluate the repeatability of the estimation when images are taken under slightly different geometrical conditions. A very good consistency between the three extracts is observed (Fig. 6) with residuals showing a normal distribution with a standard deviation of about 16.57 plants/m^2.

A more detailed inspection of the repeatability shows that it depends whether images belong to the same UAV track or not. For each subsample, the absolute values of the differences between the three image extracts noted R_x with x = [1, 2, 3] were computed, providing 3 possible couples: $\Delta_{12} = |R_1 - R_2|$, $\Delta_{13} = |R_1 - R_3|$ and $\Delta_{23} = |R_2 - R_3|$. The resulting 90 Δ_{ij} computed over the 30 subsamples available were split into three groups: image extracts belonging to the same tracks (48 couples), image extracts belonging to two adjacent tracks (27 couples) and image extracts belonging to two non-adjacent tracks (15 couples). Results (Fig. 7) show that the absolute values of the differences are smaller when the image extracts came from the same tracks with an average value of (Δ_{same} = 16.46 plants/m^2). This is explained by the geometry of observation which is relatively similar. Conversely, when image extracts come from two different tracks, the observation geometry is more variable, inducing larger differences in the plant density estimation ($\Delta_{adjacent}$ = 21.44 plants/m^2). This effect is even increased when the image extracts belong to non-adjacent tracks ($\Delta_{non-adjacent}$ = 35.20 plants/m^2) corresponding to larger differences in the observation geometry. These results suggest therefore that each subsample should be imaged with similar observational geometry to get more consistent plant density estimation.

3.3. Impact of the spatial resolution on the performances

A simulation study was first conducted to analyze the impact of the spatial resolution on the performances of the method. The Gréoux

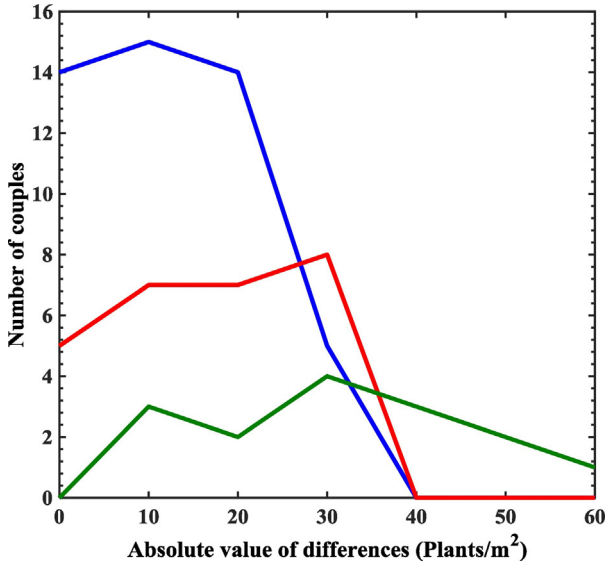

Fig. 7. Distribution of absolute value of differences between images extracts of the same subsample. The blue (respectively red and green) line corresponds to image extracts coming from the same track (respectively adjacent and non-adjacent tracks). (For interpretation of the references to color in this figure legend, the reader is referred to the web version of this article.)

experiment with its very high resolution (0.20 mm) was used for this purpose. Its original spatial resolution was degraded to 0.40, 0.60, 0.80 and 1.00 mm using a simple aggregation technique: the mean of 2 × 2, 3 × 3, 4 × 4 and 5 × 5 groups of pixels was computed. The complete data processing was applied to each of the 4 degraded spatial resolution images, including the automatic classification and the training of the PSO-SVM to identify the number of plants per image object. Results show that the estimation accuracy of the model is decreasing linearly with the spatial resolution of images (Fig. 8a). Examples of different spatial resolution images are showed in Fig. 8b. Best performances are obtained for the original 0.20 mm resolution with RMSE = 28.11 plants/m^2 and RRMSE = 15.25%. This is in good agreement with results from Liu et al. (2017) who get a spatial resolution of 0.2 mm from ground based RGB imagery. Conversely, very poor estimates are observed for the 1 mm resolution with RMSE = 93.89 plants/m^2 and RRMSE = 51.03%. When the resolution of images is degrading, the classification is less accurate, particularly when leaves from adjacent plants are close together. Further, the image objects are losing progressively details which impact the value of the features, making the identification of the number of plants per image objects more difficult.

These simulation results were verified over the Avignon site where images were acquired both at 5 m and 7 m altitude, corresponding respectively to 0.33 mm and 0.45 mm spatial resolution. The degraded spatial resolution (0.45 mm) induces a significant decrease of the performances (Fig. 9) with a difference in RMSE and RRMSE values close to 30 plants/m^2 and 10%, respectively (Table 6). The effect of the increase by 0.12 mm of the pixel size impacts more largely the performances of plant density estimation as compared to what was observed previously from the simulations on the Gréoux site. This may be explained by the slightly later Haun stage and higher plant density that makes more overlap between plants with increasing difficulties when estimating the number of plants within image objects. Note however that the bias seems almost unchanged between the 2 resolutions (Table 6). A spatial resolution of RGB images better than 0.40 mm seems required to obtain a good estimation of the plant density. These results agree with Zhang and Kovacs (2012) and Sankaran et al. (2015b) who concluded that high spatial resolution images could be better used for precision agriculture and crop phenotyping applications.

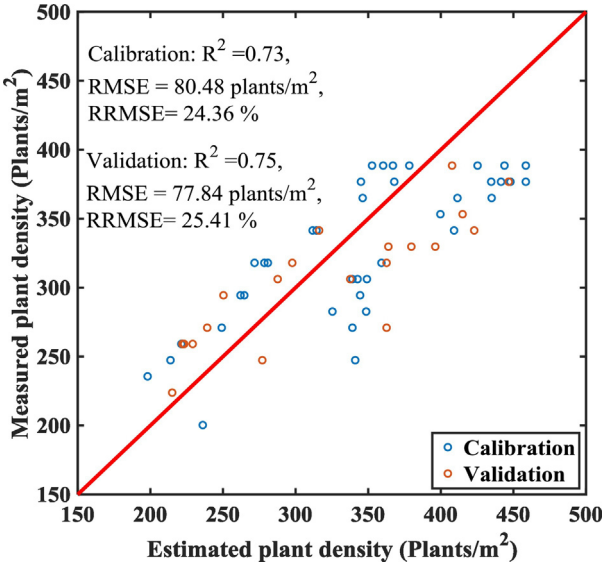

Fig. 9. Comparison between the estimated and the measured plant density for winter wheat using the 7 m height UAV imagery data at the Avignon experimental site.

4. Conclusion

This study presents a first attempt to estimate plant density of wheat crop at emergence from RGB imagery taken from a UAV. Under the variable conditions experienced, the retrieval performances of the plant density provide RMSE between 21.66 and 52.35 plants/m^2 for densities spanning from 79 to 388 plants/m^2. It corresponds to a relative RMSE values ranging from 9.24% to 17.12%, i.e. close to the 10% uncertainties often considered as the target accuracy to be reached. Best performances require a spatial resolution better than 0.40 mm to ease the classification of the green pixels and the retrieval of the number of plants per image objects made of several overlapping plants.

The needed low altitude flights induce potential source of problems for the photogrammetric techniques used to retrieve the precise positions of the cameras when the image is acquired. Alternatively, the use of an onboard centimetric accuracy geopositioning system

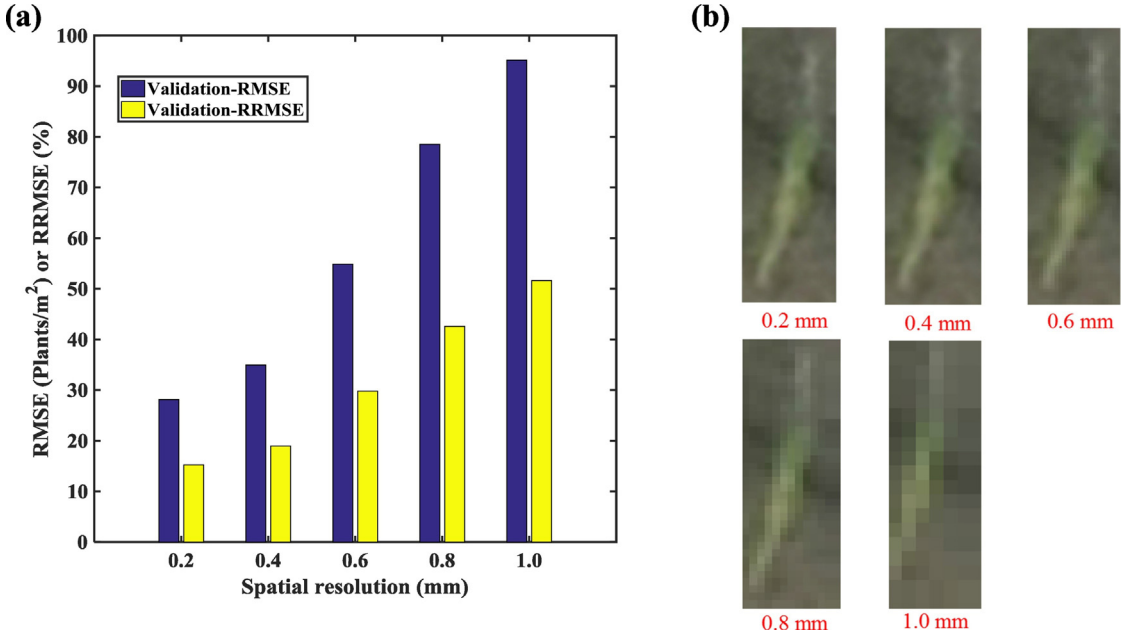

Fig. 8. The impact of different spatial resolution on the estimation accuracy of model (a) and example of different spatial resolution images (b) at the Gréoux experimental site.

Table 6
Performances of the estimation of plant density over the Avignon experimental site for the two altitudes tested.

Altitude (m)	Dataset	Sample size	Slope	Intercept	R^2	RMSE (plants/m^2)	RRMSE (%)	d	Bias (plants/m^2)
Avignon	Calibration	40	0.69	89.02	0.80	50.62	15.52	0.81	15.90
@5 m	Validation	20	0.57	121.84	0.81	52.35	17.12	0.80	15.48
Avignon	Calibration	40	0.57	133.18	0.73	80.48	24.63	0.69	15.96
@7 m	Validation	20	0.49	145.52	0.75	77.84	25.41	0.72	17.05

combined with the IMU (Inertial Measurement Unit) information on camera orientation will allow to directly project the image onto the ground surface with sufficient accuracy: because of the low altitude, the uncertainties on the orientation of the camera coming from the IMU will translate into limited positioning errors. This will considerably simplify the image acquisition and primary processing. It was also demonstrated that the geometry of observation significantly impacts the plant density estimates. Caution should therefore be taken to ensure consistent acquisition geometry over each subsample or plot. Further, the selection of the image the closest to the targeted direction is therefore a very important step. Finally, because of the relatively easy and automatic way to collect and process the images, plant density estimation could be applied over large samples: such extensive sampling area contrasts with the classical techniques based on ground measurements that are generally applied on a restricted sample size.

The method developed here requires a specific training for each new data set to account for possible changes due to the Haun stage or other acquisition conditions including wind. However, merging the individual training datasets to build a classification algorithm that associates with a good accuracy the number of plants contained in each image object will make the method much easy to use. However, this will require very efficient machine learning techniques to get robust results against the large diversity of situations encountered. In this study, we only used the original images collection for a given plot based on our developed method. However, a basic edition of the mosaic (via selecting the best images to take part in the mosaic) could also render similar results and avoid the potential shortcoming of this method while allowing an exhaustive coverage of the whole study area. Finally, the method could be adapted to other crops having relatively small elements, sown unevenly along the row and with limited spacing between plants.

Acknowledgements

This study was supported by “Programme d'investissement d'Avenir” PHENOME (ANR-11-INBS-012) and Breedwheat (ANR-10-BTR-03) with participation of France Agrimer and “Fonds de Soutien à l'Obtention Végétale”. The grant of Shouyang Liu was funded by the Chinese Scholarship Council. We thank also the people from Gréoux, Clermont and Avignon who participated to the experiments. The work was completed within the UMT-CAPTE funded by the French ministry of Agriculture.

References

Agisoft, L.L.C., 2016. Agisoft Photoscan User Manual Professional Edition, Version 1.2. Agisoft LLC, St. Petersburg, Russia Available at: http://www.agisoft.com/pdf/photoscan-pro_1_2_en.pdf (Accessed: 11.03.2016).
Ahmed, S.K., Abidin, A.A.Z., Ali, Z., Wong, B.Y., Shariff, Z.M., 2008. Image processing of a banana: area determination via edge detection using MATLAB. 4th International Colloqium on Signal Processing and Its Applications, Kuala Lumpur.
Araus, J.L., Cairns, J.E., 2014. Field high-throughput phenotyping: the new crop breeding frontier. Trends Plant Sci. 19, 52–61.
Bendig, J., Yu, K., Aasen, H., Bolten, A., Bennertz, S., Broscheit, J., Gnyp, M.L., Bareth, G., 2015. Combining UAV-based plant height from crop surface models, visible, and near infrared vegetation indices for biomass monitoring in barley. Int. J. Appl. Earth Obs. 39, 79–87.
Díaz-Varela, R.A., de la Rosa, R., León, L., Zarco-Tejada, P.J., 2015. High-resolution airborne UAV imagery to assess olive tree crown parameters using 3D photo reconstruction: application in breeding trials. Remote Sens. 7, 4213–4232.
Ehsani, R., Maja, J.M., 2013. The rise of small UAVs in precision agriculture. Resour. Mag. 20, 18–19.
Furbank, R., Tester, M., 2011. Phenomics - technologies to relieve the phenotyping bottleneck. Trends Plant Sci. 16, 635–644.
Gómez-Candón, D., De Castro, A., López-Granados, F., 2014. Assessing the accuracy of mosaics from unmanned aerial vehicle (UAV) imagery for precision agriculture purposes in wheat. Precis. Agric. 15, 44–56.
Guillen-Climent, M., Zarco-Tejada, P.J., Berni, J.A., North, P., Villalobos, F., 2012. Mapping radiation interception in row-structured orchards using 3D simulation and high-resolution airborne imagery acquired from a UAV. Precis. Agric. 13, 473–500.
Haralick, R.M., Shapiro, L.G., 1992. Computer and Robot Vision, 1. Addison-Wesley, pp. 28–48.
Haun, J.R., 1973. Visual quantification of wheat development. Agron. J. 65, 116–119.
Hough, P.V.C., 1962. Method and means for recognizing complex patterns. U.S. Patent 3069654.
Hunt, E.R., Cavigelli, M., Daughtry, C.S., Mcmurtrey III, J.E., Walthall, C.L., 2005. Evaluation of digital photography from model aircraft for remote sensing of crop biomass and nitrogen status. Precis. Agric. 6, 359–378.
Hunt, E.R., Hively, W.D., Daughtry, C.S.T., McCarty, G.W., Fujikawa, S.J., Ng, T.L., Linden, D.S., Yoel, D.W., 2008. Remote sensing of crop leaf area index using unmanned airborne vehicles. Proceedings of the Pecora 17 Symposium, Denver, CO.
Hunt, E.R., Hively, W.D., Fujikawa, S.J., Linden, D.S., Daughtry, C.S.T., McCarty, G.W., 2010. Acquisition of NIR-green-blue digital photographs from unmanned aircraft for crop monitoring. Remote Sens. 2, 290–305.
Jia, J., Krutz, G.W., Gibson, H.W., 1991. Corn plant locating by image processing, Fibers' 91, Boston, MA. Int. Soc. Opt. Photon. 246–253.
Jin, J., Tang, L., 2009. Corn plant sensing using real-time stereo vision. J. Field Robot. 26, 591–608.
Joseph, K., Alley, M., Brann, D., Gravelle, W., 1985. Row spacing and seeding rate effects on yield and yield components of soft red winter wheat. Agron. J. 77, 211–214.
Kenndy, J., Eberhart, R., 1995. Particle swarm optimization. Proceedings of IEEE International Conference on Neural Networks, pp. 1942–1948.
Liu, S.Y., Baret, F., Andrieu, B., Burger, P., Hemmerlé, M., 2017. Estimation of wheat plant density at early stages using high resolution imagery. Front. Plant Sci. 8:739. http://dx.doi.org/10.3389/fpls.2017.00739.
Maertens, K., Reyns, P., De Clippel, J., De Baerdemaeker, J., 2003. First experiments on ultrasonic crop density measurement. J. Sound Vib. 266, 655–665.
Meyer, G.E., Neto, J.C., 2008. Verification of color vegetation indices for automated crop imaging applications. Comput. Electron. Agric. 63, 282–293.
Mountrakis, G., Im, J., Ogole, C., 2011. Support vector machines in remote sensing: a review. ISPRS J. Photogramm. 66, 247–259.
Nakarmi, A.D., Tang, L., 2012. Automatic inter-plant spacing sensing at early growth stages using a 3D vision sensor. Comput. Electron. Agric. 82, 23–31.
Nakarmi, A.D., Tang, L., 2014. Within-row spacing sensing of maize plants using 3D computer vision. Biosyst. Eng. 125, 54–64.
Otsu, N., 1979. A threshold selection method from gray-level histogram. IEEE Trans. Syst. Man Cybern. 9, 62–66.
Saeys, W., Lenaerts, B., Craessaerts, G., De Baerdemaeker, J., 2009. Estimation of the crop density of small grains using LiDAR sensors. Biosyst. Eng. 102, 22–30.
Sankaran, S., Khot, L.R., Carter, A.H., 2015a. Field-based crop phenotyping: Multispectral aerial imaging for evaluation of winter wheat emergence and spring stand. Comput. Electron. Agric. 118, 372–379.
Sankaran, S., Khot, L.R., Espinoza, C.Z., Jarolmasjed, S., Sathuvalli, V.R., Vandemark, G.J., Miklase, P.N., Carterf, A.H., Pumphrey, M.O., Knowles, N.R., et al., 2015b. Low-altitude, high-resolution aerial imaging systems for row and field crop phenotyping: a review. Eur. J. Agron. 70, 112–123.
Shi, Y., Wang, N., Taylor, R.K., Raun, W.R., 2015. Improvement of a ground-LiDAR-based corn plant population and spacing measurement system. Comput. Electron. Agric. 112, 92–101.
Shrestha, D.S., Steward, B.L., 2003. Automatic corn plant population measurement using machine vision. Trans. ASAE 46, 559.
Shrestha, D.S., Steward, B.L., 2005. Shape and size analysis of corn plant canopies for plant population and spacing sensing. Appl. Eng. Agric. 21 (2), 295–303.
Sullivan, D., Fulton, J., Shaw, J., Bland, G., 2007. Evaluating the sensitivity of an unmanned thermal infrared aerial system to detect water stress in a cotton canopy. Trans. ASABE 50, 1963–1969.
Tang, L., Tian, L.F., 2008a. Plant identification in mosaicked crop row images for automatic emerged corn plant spacing measurement. Trans. ASABE 51, 2181–2191.
Tang, L., Tian, L.F., 2008b. Real-time crop row image reconstruction for automatic emerged corn plant spacing measurement. Trans. ASABE 51, 1079–1087.
Vapnik, V., 2013. The Nature of Statistical Learning Theory. Springer Science & Business Media.
Vapnik, V.N., Vapnik, V., 1998. Statistical Learning Theory, 1. Wiley, New York.

Verger, A., Vigneau, N., Chéron, C., Gilliot, J.M., Baret, F., 2014. Green area index from unmanned aerial system over wheat and rapeseed crops. Remote Sens. Environ. 152, 654–664.
Walter, A., Liebisch, F., Hund, A., 2015. Plant phenotyping: from bean weighing to image analysis. Plant Methods 11, 1–11.
Whaley, J., Sparkes, D.L., Foulkes, M.J., Spink, J.H., Semere, T., Scott, R.k., 2000. The physiological response of winter wheat to reductions in plant density. Ann. Appl. Biol. 137, 165–177.
Willmott, C.J., 1982. Some comments on the evaluation of model performance. Bull. Am. Meteorol. Soc. 11, 1303–1313.
Wilson, P.D., Sagan, C., 1995. Spectrophotometry and organic matter on Iapetus: 1. Composition models. J. Geophys. Res. Planets 100, 7531–7537.
Zarco-Tejada, P.J., González-Dugo, V., Berni, J.A., 2012. Fluorescence, temperature and narrow-band indices acquired from a UAV platform for water stress detection using a micro-hyperspectral imager and a thermal camera. Remote Sens. Environ. 117, 322–337.
Zarco-Tejada, P.J., Guillén-Climent, M.L., Hernández-Clemente, R., Catalinac, A., Gonzálezc, M.R., Martínc, P., 2013. Estimating leaf carotenoid content in vineyards using high resolution hyperspectral imagery acquired from an unmanned aerial vehicle (UAV). Agric. For. Meteorol. 171, 281–294.
Zhang, C., Kovacs, J.M., 2012. The application of small unmanned aerial systems for precision agriculture: a review. Precis. Agric. 13, 693–712.

View publication stats